Effective Anisotropy in Fe-Ni nanowire arrays with strong dipolar interaction

Joaquín Almeira,[1,2] Fernando Meneses,[1,2] Julián Milano,[3] Carlos Ramos,[3]

Silvia E. Urreta,[1] Paula G. Bercoff[1,2]

[1]Facultad de Matemática, Astronomía, Física y Computación. Universidad Nacional de Córdoba. Ciudad Universitaria, 5000 Córdoba, Argentina.

[2]Instituto de Física Enrique Gaviola. Conicet. Ciudad Universitaria, 5000 Córdoba, Argentina.

[3]Instituto de Nanociencia y Nanotecnología, CNEA-CONICET, Centro Atómico Bariloche, 8400, San Carlos de Bariloche, Río Negro, Argentina.

Corresponding Author: Paula G. Bercoff, E-mail: bercoff@famaf.unc.edu.ar

Abstract

The effective magnetic anisotropy field H_{eff} of $Fe_x Ni_{(100-x)}$ (x = 15, 25, and 38) nanowires of 65 nm diameter forming ordered arrays within dense alumina templates of ~35% porosity, was determined. Different values for H_{eff} were obtained depending on the determination method, which were: magnetization evolution along major hysteresis loops; ferromagnetic resonance at 34 GHz; and magnetization switching by curling nucleation (through angular variation of the coercive field). H_{eff} values determined from magnetization measurements differ from those arising from FMR measurements, being these latter quite smaller in every case. No evidence of an easy plane behavior was found, as theoretically predicted for high porosity arrays as ours.
These results suggest that new internal degrees of freedom need to be considered for the effective anisotropy description in quasistatic hysteresis loops, during polarization reversal and in ferromagnetic resonance dynamic processes, to understand and model these experimental findings. We discuss possible causes.

Keywords: Permalloy; nanowires; magnetic anisotropy; dipolar interaction

1. Introduction

Originally, Permalloy was the trademark registered by Bell Laboratories [1] for the specific composition of iron-nickel alloy with precisely 78.5 at. % Ni. However, magnetic iron-nickel alloys with *fcc* structure and ~20-30 Ni at. % are generally known as permalloys [2]. Alloys close to this composition have quite low crystalline anisotropy and magnetostriction constants, which can even be zero for certain Ni percentages, making these compounds some of the softest magnetic materials. Moreover, low coercivity is a remarkable feature of permalloys, since even almost a century after their discovery, it is still not completely understood how the material's constants originate this behavior [3, 4]. Thence, this system has peculiarities worth studying. In addition, other permalloys with lower Ni content possess properties of technical interest which are also appealing to investigate [5].

In recent years, with the advent of new techniques for visualization and manipulation of nanomaterials, researchers have tried to transfer the known bulk ferromagnetic properties ─like those of permalloys─ to different nanostructures, motivated by the unique

properties related to surface-, small size-, and quantum-effects present in these structures. Arrays of ferromagnetic nanowires (NWs) have been attracting considerable attention due to the outstanding magnetic features associated to their cylindrical symmetry and collective response that can be profited for applications in several technologies. Great progress has been made in spintronics [6] as well as attempts of controlling magnetic domain configurations, for instance with multilayered NWs [7], to obtain better magnetic recording [8] performances. Some NWs advantages such as small size scale, large aspect ratio or large specific area have led to the design of devices like electrochemical sensors and biosensors [9, 10] as well as electrochemical energy storage devices [11]. The high magnetization, relatively low cost and effective synthesis of NWs also enable the use of innovative techniques for biomedical applications [12] or for environmental remediation [13].

In an array of ordered NWs, the magnetism of individual NWs determines the most relevant properties of the ensemble. The magnetic response of each NW is a function of a uniaxial anisotropy arising from the NWs large aspect ratio (shape anisotropy) and the magnetocrystalline anisotropy, both depending on the composition. These contributions exhibiting uncommon magnetic textures lead to quite interesting behaviors. However, the resulting array properties may be largely modified by the interwire magnetostatic interactions.

Considering that magnetocrystalline anisotropy in Permalloys is negligible, the magnetic behavior of the array becomes governed by an effective anisotropy K_{eff} defined by the interplay of the shape anisotropy of each NW in the array and a magnetostatic contribution arising from the dipolar interwire interaction, which depends on the NWs alloy saturation magnetization, their diameter and the mean distance between the NWs, defined in principle by the template porosity P and the filling factor. Most of the previously reported results regarding magnetic microstructures and hysteresis properties of Fe-Ni NWs [14, 15] involve arrays with relatively low porosity values, where only small contributions of interwire dipolar interaction to the array behavior are expected. For effective uniaxial anisotropy determinations in arrays with high wire packing density, FMR techniques have been widely used. It is shown [16-20] that by modifying the wire packing density, the dispersion relation can change from strongly dependent to quasi-independent on the applied field direction. This effect is explained in terms of the dipolar coupling between wires which competes with the individual NW shape anisotropy, leading to an effective anisotropy which can be easily tunable by selecting the template porosity and the material's saturation magnetization. These facts illustrate the quite complex nature of this effective parameter in Fe-Ni NW arrays.

In this work, the effective anisotropy constant K_{eff} is determined for Fe-Ni NW arrays of compositions $Fe_x Ni_{(100-x)}$ (x = 15, 25, 38), exhibiting high saturation magnetization, small magnetocrystalline anisotropy and magnetostriction values, and morphologies promoting relatively large interwire dipolar interaction (high porosity (35%), large wire diameter and length, and efficient pore filling). The effective anisotropy fields related to the samples' effective anisotropies are measured in three different scenarios, involving the interaction of magnetization with an external magnetic field: a) performing the quasistatic magnetization evolution along the major hysteresis loop M(H), b) using ferromagnetic resonance, and c) measuring the magnetization switching which is responsible for the observed coercive field H_C angular dependence. It is found that the effective anisotropy value depends not only on porosity and composition, but also on the process selected for its determination. Possible causes of these results are considered.

2. Experimental procedures

2.1. Nanoporous alumina membranes

Patterned templates made of nanoporous alumina membranes with tubular, hexagonally self-assembled nanopores were synthesized by the conventional two-step anodization process [21] performed on high-purity aluminum foils (Al 99.997\%, Alfa Æsar).

Before the first anodization process, the foils were flattened with a hydraulic press, sonicated in ethanol and acetone, and then electropolished by electrolysis in a mixture of $HClO_4$ + ethanol 1:3 applying a continuous voltage of 20 V versus a graphite counter electrode, for 2.5 min at room temperature. After the foil surface roughness was reduced and mirror-like surfaces were obtained, the Al substrates were anodized in a 0.3 M oxalic acid (H_2C_2O4) aqueous solution for 4 h at ~1 °C under an applied continuous voltage of 40 V. The so-formed alumina layer was dissolved in a 0.4 M H_3PO_4 + 0.3 M CrO_3 aqueous solution at room temperature for about 4 days. After that, the substrates were again anodized for 23 h under the same conditions than the first anodization. A highly ordered, hexagonal array of nanopores was obtained. The remaining Al substrate was removed in a 0.1 M $CuCl_2.2H_2O$ + 3 M

HCl aqueous solution to expose the insulating alumina barrier layer at the bottom of the pores, which was consecutively opened by chemical etching, in a diluted 5 wt.% H_3PO_4 aqueous solution at 32 °C for 30 min. This procedure also slightly increases the diameter of the pores without altering their ordered structure, as shown in Figure 1a.

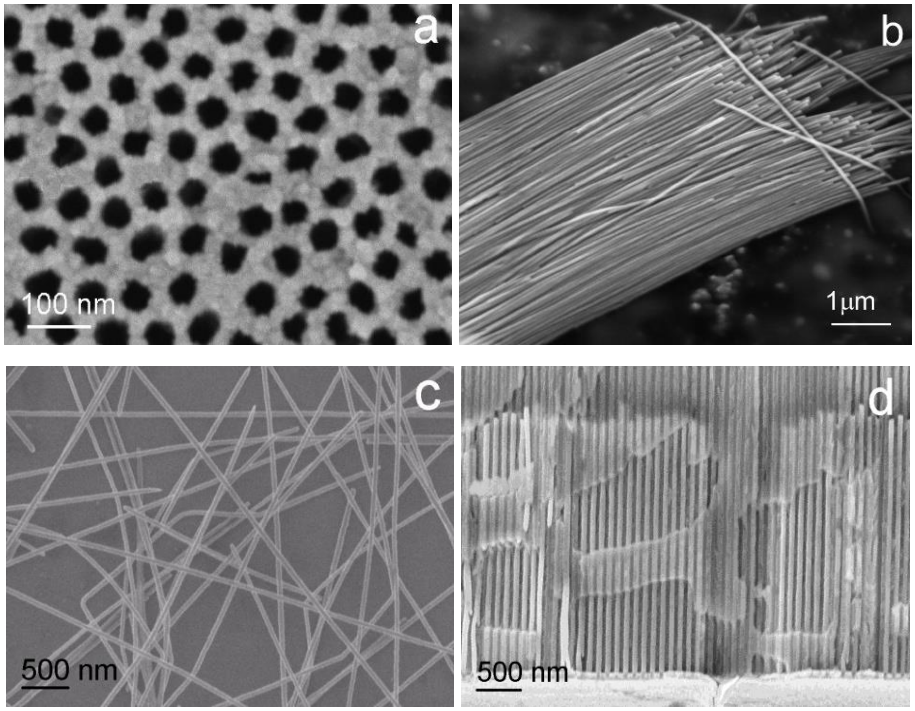

Figure 1. (a) Anodized alumina template after pore widening, rendering 65 nm diameter pores and 35% porosity. (b) Fe15 and (c) F25 NWs released from the template and (d) Fe38 NW array.

The final parameters determining the membrane characteristics are pore's diameter D = (65±5) nm, and the center-to-center distance d_{cc} = (105 ± 5) nm, leading to a D/d_{CC} ratio of S = D/d_{CC} = 0.62 ± 0.06 and a porosity P = (35 ± 6) % (where P is defined as $P = \pi/2\sqrt{3}(D/d_{cc})^2$ [22])

A conductive gold layer of 60 nm was sputtered on the bottom of the membrane to serve as a working electrode. This gold coating is resistant to oxidation and does not provide appreciable magnetic signal.

2.2. Electrodeposition of Fe-Ni NWs

The electrodeposition of Fe-Ni NWs was performed using a three-electrode setup in a Teflon electrochemical cell, equipped with an Ag/AgCl reference electrode, a Pt counter electrode, and the gold layer of the nanoporous alumina membrane acting as a working electrode. The deposition process was carried out in a 0.027 M $FeSO_4.7\ H_2O$ + 0.43 M $NiSO_4.6H_2O$ + 0.36 M H_3BO_3 + 0.75 mM $C_6H_8O_6$ aqueous solution at room temperature. The boric acid is incorporated to enhance the conductivity and the ascorbic acid to avoid iron oxidation. Before each deposition, oxygen was purged from the solution by moderate nitrogen bubbling to reduce the risk of oxidation without producing large convective currents.

The NWs composition was controlled by selecting the applied voltage as indicated in Table 1. The mean composition of the different arrays was determined by the EDS technique. Many zones were measured in each sample and the mean at. % iron (balance Ni) and deviation values were estimated. Details of the composition determination are given in the Supplementary Information section. Throughout this work, the samples will be denoted according to their iron composition, that is, Fex ≡ Fe_xNi_{100-x} (x = 15, 25, 38).

SEM images are displayed in Figure 1 for samples (b) Fe15, (c) Fe25 and (d) Fe38, resulting from the different synthesis conditions. The NWs replicate the pores cylindrical shape, with a mean diameter D = (65

± 5) nm and different lengths L according to the synthesis parameters, leading to large aspect ratios ($A_R = L/D > 50$) in every case (Table 1).

Table 1. Sample denomination, the corresponding atomic composition, the voltage V_{ED} used for electrodeposition, together with the lattice parameter a, the Scherrer crystallite size d_S and the mean aspect ratio A_R of the different NW arrays, are listed.

Sample	Fe15	Fe25	Fe38
Composition	$Fe_{15}Ni_{85}$	$Fe_{25}Ni_{75}$	$Fe_{38}Ni_{62}$
V_{ED} [V]	-1.4	-1.3	-1.0
a [Å]	3.542	3.547	3.562
d_S [nm]	18	14	8
A_R	260	270	50

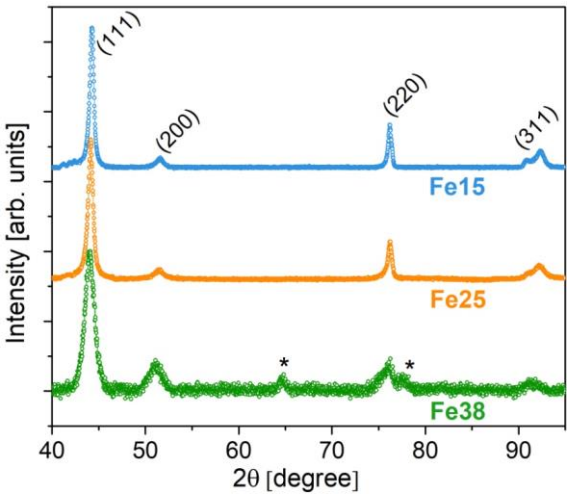

Figure 2. XRD patterns corresponding to samples of the different NW arrays. NWs are nanocrystalline and single phase. The reflection peaks could be indexed considering a polycrystalline *fcc* γNi(Fe) cubic structure. The asterisk in the last pattern corresponds to peaks arising from the sample holder.

3. Results and discussion

3.1 Microstructure

The NWs crystalline structure was determined by X-Ray Diffraction (XRD), in a Panalytical X'Pert Pro diffractometer, using Cu-Kα radiation. These measurements were performed keeping the NWs inside the amorphous AAO templates to preserve their order; each array was placed on an aluminum holder, being the incidence plane perpendicular to the wires' axis. The XRD patterns are shown in Figure 2, where only the peaks corresponding to a disordered *fcc* γNi(Fe) cubic structure can be observed. In one of the patterns, small reflections from the Al sample holder are also noticed.

For all samples, the Scherrer crystallite sizes [23] d_S were calculated, and the lattice constants were experimentally determined from the Bragg's law and the lattice geometry [24]. These parameters are listed in Table 1. From these results it is possible to conclude that all the samples are polycrystalline (nanocrystalline) and single phase, with no preferred grain orientation.

3.2 Magnetic characterization

Hysteresis properties

Figure 3 displays the room temperature hysteresis loops corresponding to the different arrays, measured in a VSM magnetometer, with the magnetic field applied along the NWs axis $\varphi = 0°$, (parallel configuration, denoted PA) and perpendicularly to this direction, $\varphi = 90°$ (perpendicular configuration, denoted PE). All samples are soft ferromagnetic, with relatively large coercivities $\mu_0 H_C$ (value at which $M = 0$) when measured along the easy axis direction (PA). It may be observed that these PA loops display a noticeable slope, indicating that the demagnetizing factor of the arrays is not negligible in this field configuration [5]. The corresponding hysteresis parameters are listed in Table 2.

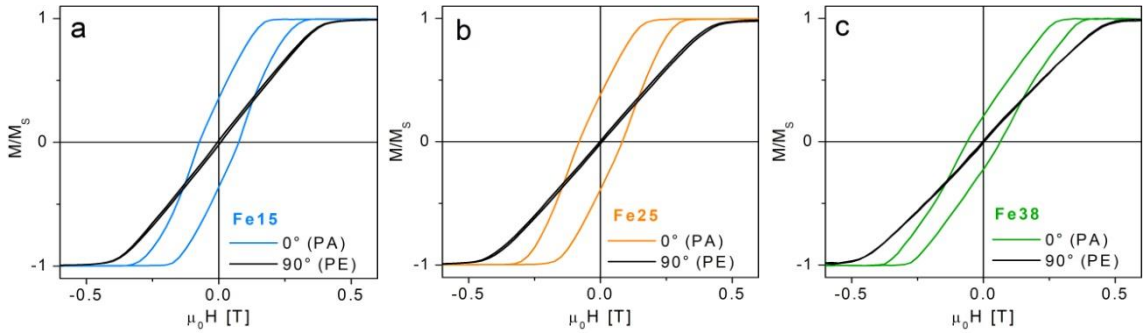

Figure 3. Room temperature hysteresis loops measured with the applied field parallel (PA) and perpendicular (PE) to the individual NWs axis. (a) Fe15, (b) Fe25 and (c) Fe38.

Table 2. Room temperature values of the coercive field $\mu_0 H_C$ (M = 0) and relative remanence M_R/M_S, obtained from the loops measured in PA configuration. The saturation magnetization values M_S^*, the magnetocrystalline energy constants K_{MC} and the corresponding shape anisotropy constants K_{Shape} are taken from [5]. Effective uniaxial anisotropy fields: $\mu_0 H^L$, estimated from the area enclosed by the hysteresis loops in Figure 3; $\mu_0 H^{FMR}$, determined from FMR measurements, by non-linear least-square fit of the experimental data to Eq. (6). The number in parenthesis indicates the statistical error of the last significant digit, and g is the gyromagnetic factor. The effective uniaxial anisotropy field $\mu_0 H^S$ acting during the major polarization switching event, and the apparent demagnetizing factors of the nucleus, $n\parallel$ and $n\perp$, as estimated by fitting Eq. (9) to the data shown in Figure 6, are also included.

Sample	Fe15	Fe25	Fe38
$\mu_0 H_C$ [mT]	90(8)	86(8)	81(8)
M_R/M_S	0.44(3)	0.41(3)	0.30(5)
$\mu_0 M_S^*$ [T]	0.9	1.2	1.5
K_{MC} [10^3 J m^{-3}]	-1	0.1	0.8
K_{Shape} [10^3 J m^{-3}]	172	286	448
$\mu_0 H^L$ [mT]	278	325	243
K^L [10^3 J m^{-3}]	125	195	182
$\mu_0 H^{FMR}$[mT]	82(3)	206(2)	146(2)
K^{FMR} [10^3 J m^{-3}]	30	98	87
g	2.12(1)	2.10(1)	2.10(1)
$\mu_0 H^S$ [mT]	350	377	268
K^S [10^3 J m^{-3}]	130	180	160
N_{eff}	- 0.13	- 0.13	- 0.07
$n\parallel$	0.16	0.18	0.13
$n\perp$	0.42	0.41	0.44

As previously commented, the contribution of the magnetocrystalline anisotropy to coercivity may be neglected. In fact, magnetocrystalline anisotropy constants K_{MC} for disordered *fcc* γFe(Ni) bulk alloys are two orders of magnitude lower than those associated to the individual NWs shape anisotropy [5, 25] —see Table 2—, indicating that the effective uniaxial anisotropy K_{eff} in the arrays arises from shape and dipolar interaction contributions.

The effective uniaxial anisotropy constant K^L may be estimated from the hysteresis loops in Figure 3, by applying the area method [26], based on the amount of energy stored in the NWs when they are magnetized to saturation in a hard direction. The effective anisotropy constant K^L and the corresponding field $\mu_0 H^L$ for each array determined by this method (area enclosed by the upper branch of the PA and PE hysteresis loops) are listed in Table 2.

Ferromagnetic resonance

FMR is a very useful tool to measure magnetic anisotropy. To eliminate contributions from different magnetic domains, FMR is usually carried out in magnetically saturated samples. To meet this condition in our samples, we performed the experiments at 34 GHz, in an ESR300 Bruker spectrometer placing the sample in the center of rectangular cavity at room temperature. The observed resonance fields $\mu_0 H_r$ lie in the range $0.9 - 1.2$ T, well above the saturation fields (< 0.5 T) as observed in $M(H)$ hysteresis loops.

Considering polar and azimuthal angles of the applied field, θ_H (fixed at $\pi/2$) and φ_H, respectively (as illustrated in Figure 4), the equilibrium direction of the magnetization is given by (θ, φ) [27, 28]. Then, the magnetic free energy per unit volume *E*, can be expressed as a function of the external magnetic field *H* as:

$$E(\theta,\varphi) = -\mu_0 H M_s \sin\theta \cos(\varphi - \varphi_H) - K_{eff} \sin^2\theta \cos^2\varphi, \quad (1)$$

where [29],

$$K_{eff} = \frac{\mu_0 M_s^2}{4}(1 - 3P) \quad (2)$$

with K_{eff} the effective uniaxial anisotropy constant taking into consideration the shape anisotropy and the dipolar interaction between NWs with large aspect ratio, as it is our case. The factor *P* is the template porosity, estimated as $P = 0.35 \pm 0.06$ from SEM images, and it is assumed that all the pores are filled with NWs.

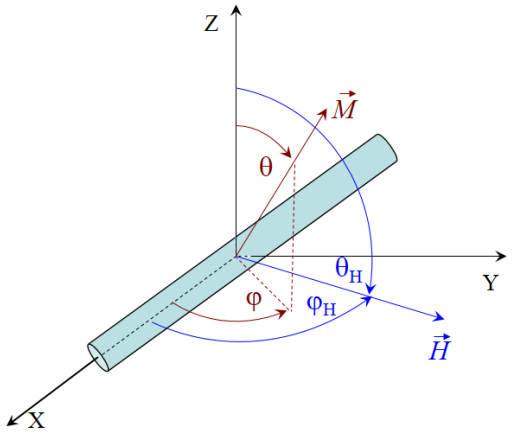

Figure 4. Schematic representation of a single nanowire and the convention used for polar and azimuthal angles of $\vec{M}(\theta,\varphi)$ and $\vec{H}(\theta_H = \pi/2, \varphi_H)$.

The pre-factor of Eq. (2) yields an estimate of the energy associated to shape anisotropy for an isolated NW: 172 kJ/m^3, 286 kJ/m^3, and 448 kJ/m^3 for Fe15, Fe25 and Fe38 respectively, where values of the saturation magnetization from its bulk values [5] were used. In Eq. (1) a crystalline anisotropy contribution is not considered because of the intrinsic low values observed in these alloys and the fact that the crystallites in the NWs are randomly oriented (as shown by XRD). Magnetoelastic energy terms are also disregarded since the samples were grown near room temperature, so strains related to differential expansion between AAO, and the NW are expected to be negligible [30].

In dense NW arrays, such as the ones considered here, dipolar interaction significantly changes the magnitude of the effective field acting on the NWs due to demagnetizing effects [29]. This dipolar interaction field can change an easy axis pointing along the wire axis towards another one lying in the normal plane, leading to an easy-plane-like behavior [15, 31]. In the present case, if the measured porosity value of *P* = 0.35(6) is introduced in Eq. (2), the onset of an easy-plane anisotropy is predicted. However, FMR and DC magnetization measurements both indicate that all the arrays still exhibit an easy-axis anisotropy.

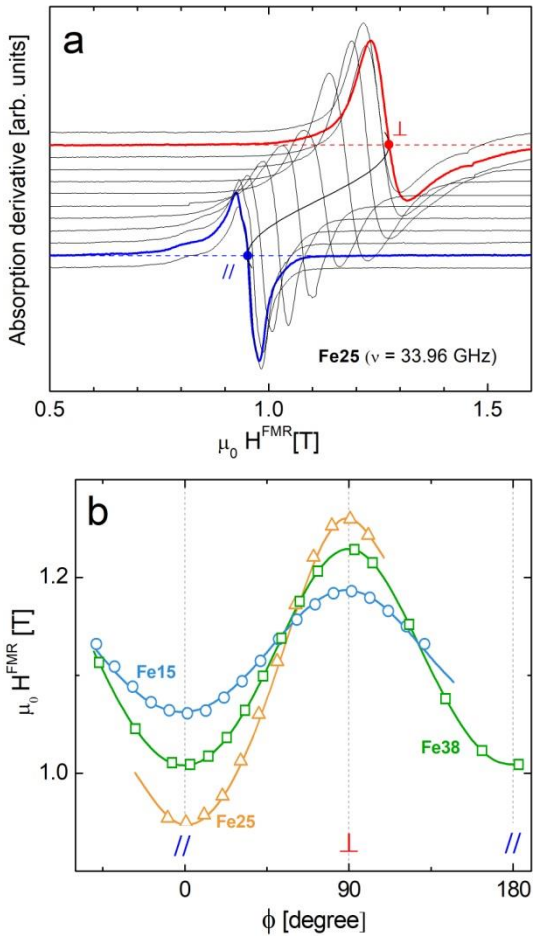

Figure 5. (a) FMR absorption derivative recorded as a function of the applied field, and the angle between the applied field and the NW axis, φ_H for sample Fe25. The spectra were obtained varying φ_H from -10º to 100º. The spectra nearest to the parallel and perpendicular directions are indicated in blue and red, respectively. (b) Magnetic resonance field as a function of φ_H for the three samples studied. The solid lines are non-linear least-square fits to data using Eq. (6) and the results are given in Table 2.

As previously indicated, a magnitude usually employed to characterize the strength of the uniaxial anisotropy is the effective anisotropy field, H_{eff}. At a given applied field, H, the magnetic moment orientation is determined from minimization of the energy with respect to θ and φ:

$$E_\theta = 0 \implies \theta = \frac{\pi}{2}$$

$$E_\varphi = 0 \implies \mu_0 H M_s \sin(\varphi - \varphi_H) + 2K_{eff} \sin\varphi\cos\varphi = 0 \quad (3)$$

which needs to be solved numerically, except for two conditions: parallel or perpendicular to the anisotropy axis. For resonance events, $K_{eff} = K^{FMR}$ in Eq. (3) . Considering $K^{FMR} > 0$ (easy axis along the NW), for $\varphi_H = 0$, $\varphi = 0$ ($\vec{M} \parallel \vec{H}$) and $\varphi_H = \pi/2$ ($\vec{H} \perp$ to the NW), Eq. (3) can be expressed as:

$$\sin\varphi = \frac{H}{H^{FMR}}; \quad H < H^{FMR} \qquad (4)$$

where $H^{FMR} = 2\,K^{FMR}/(\mu_0 Ms)$ is the anisotropy field. This model predicts that the measured magnetic moment is proportional to the applied field up to the anisotropy field at which $M = M_S$ and $\varphi = \varphi_H$, similar to what is the observed in the $M(H)$ data (Fig. 3) [27].

Ferromagnetic resonance is given by:

$$\frac{\omega}{\gamma} = \frac{1}{\mu_0 M_S \sin\theta}\left[E_{\theta\theta}E_{\varphi\varphi} - E_{\theta\varphi}^2\right]_{eq}^{1/2} \qquad (5)$$

where $E_{ij} = \frac{\partial^2 E}{\partial i \partial j}$ and Eq. (5) is evaluated at the equilibrium angles given by Eq. (3). The angular variation of the FMR spectra is given by:

$$\frac{\omega}{\gamma} = \sqrt{[H\cos(\varphi - \varphi_H) + H^{FMR}\cos^2\varphi][H\cos(\varphi - \varphi_H) + H^{FMR}\cos 2\varphi]} \qquad (6)$$

where $\omega = 2\pi\nu$ and $\gamma = \frac{g\mu_B}{\hbar}$; ν = 33.96 GHz is the microwave frequency used and g is the gyromagnetic ratio. In the case of $\vec{H}$ ∥NW ($\varphi_H = 0$) Eq. (6). reduces to $\frac{\omega}{\gamma} = H_\parallel + H^{FMR}$ and for $\vec{H} \perp$ NW, it is $\frac{\omega}{\gamma} = \sqrt{H_\perp(H_\perp - H^{FMR})}$. Figure 5 depicts a typical angular variation of the magnitudes from which the value of the effective anisotropy and g-factors are determined. The resulting values are shown in Table 2.

Magnetization mechanisms

Another route to estimate the effective uniaxial anisotropy field of the NWs array is the analysis of the magnetization reversal process. It is known that the angular dependence of the coercive field and remanence are related to the prevailing magnetization mechanism operating in the NW array and this mechanism is closely related to the effective anisotropy field acting during this dynamic process. The magnetization reversal of an ordered array of magnetic NWs is generally modeled considering the mechanisms acting in individual NWs ─dependent on geometry, size, composition, and microstructure─ and the dipolar magnetic interaction among NWs in the array. The magnitude of these interactions also depends on composition, size, and geometry of the individual nanowires but it is largely determined by

the template porosity and the fraction of pores filled during electrodeposition.

In these polycrystalline, relatively large nanowires, delocalized reversal modes may be excluded [32], so local microstructure features and/or local internal fields become important. Then, a description based on the nucleation of inverse domains and the further displacement of the domain walls will be assumed. The formation of these initial inverse domains may proceed by local coherent rotation [33] or curling [34] in the nucleus volume, being the latter mode quite efficient in magnetically soft materials as in the present case. Atomic defects such as NWs irregular ends, zones of fluctuating wire diameter and grain boundaries, all act as nucleation catalyzers. The best suited mechanism for magnetically soft NWs of intermediate diameter (50 nm < D < 100 nm), is that in which inverse domains nucleate by localized curling and then the new formed vortex-like domains further expand though many grains [35, 36]. Then, the angular dependence of the coercive field controlled by the nucleation of such inverse nucleus by a curling/vortex-like process may be expressed, ignoring as before the angular dependence of the dipolar field, as:

$$\mu_0 H_C = -\mu_0 \frac{2K^S}{J_s} + N_{eff} J_S \qquad (8)$$

$$\mu_0 H_C(\phi) = \mu_0 \frac{2K^S}{J_s} \frac{\left(n_{\parallel} - \frac{q^2 L_x^2}{R^2}\right)\left(n_{\perp} - \frac{q^2 L_x^2}{R^2}\right)}{\sqrt{\left(n_{\parallel} - \left(\frac{q^2 L_x^2}{R^2}\right)^2\right) sin^2\phi + \left(n_{\perp} - \frac{q^2 L_x^2}{R^2}\right)^2 cos^2\phi}} + N_{eff} J_S \qquad (9)$$

Here, J_S=$\mu_0 M_S$ is the saturation magnetic polarization; $R = \frac{D}{2}$ is the mean wire radius and $L_x = \sqrt{\frac{2A\mu_0}{J_S^2}}$ is the exchange length, which is composition-sensitive through J_S values; A is the exchange energy constant and K^S is the effective uniaxial anisotropy constant associated to the dynamic reversal process; $q^2 = 1.08\pi$ [37] is a geometry-related constant; $n_{\parallel}$ and $n_{\perp}$ are the nucleus demagnetizing factors parallel and perpendicular to the NW axis, respectively, with $n_{\parallel} + 2\, n_{\perp} = 1$.

In many systems the observed reversal mechanism is not described by Eq. (9) because of the different scenario and energetic provided by NW microstructure and composition.

The second term in the right hand of Eq. (9) is a mean value of the dipolar interaction contribution to the coercive field, for applied fields forming angles between 0 and $\pi/2$ with the NWs axis.

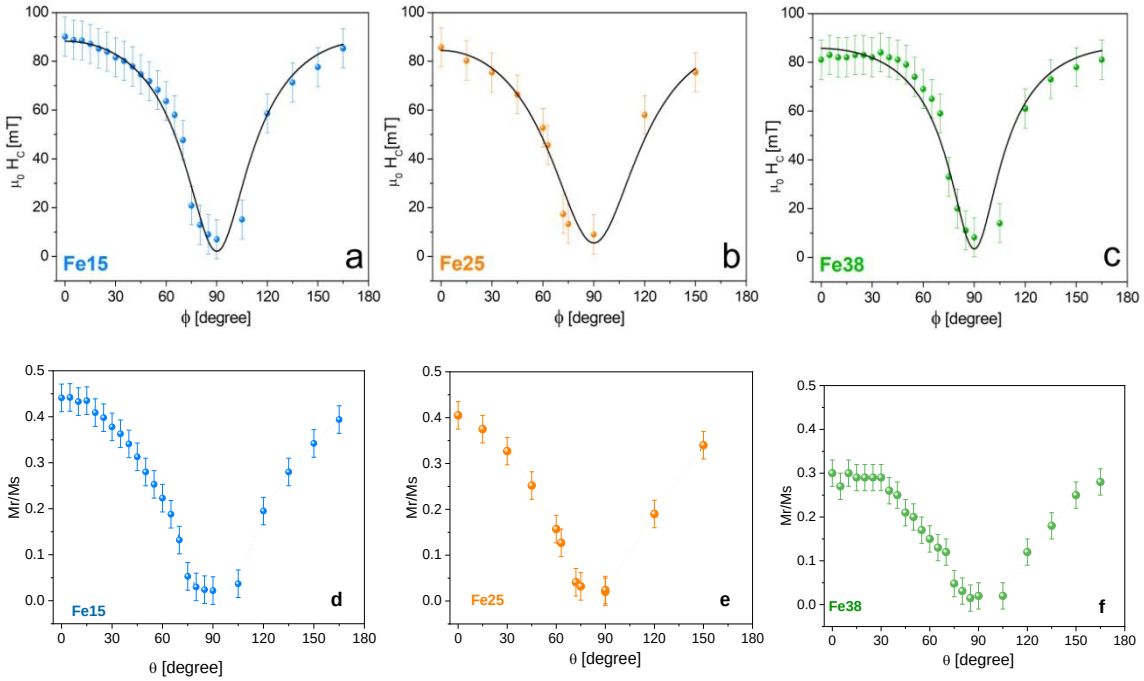

Figure 6. Angular dependence of the coercive field $\mu_0 H_C$ and the relative remanence M_R/M_S for the NW arrays investigated: (a,d) Fe15, (b,e) Fe25, and (c,f) Fe38. The solid lines in $\mu_0 H_C$ plots correspond to fits of Eq. (9) to the experimental data. Dotted lines in M_R/M_S curves are only a guide.

Figure 6 illustrates the experimental data for the orientation dependence of the coercive field and the relative remanence in the investigated NW arrays; the solid lines in the $\mu_0 H_C$ plots correspond to the behaviors predicted by Eq. (9) for the different samples. The main parameters resulting from the best fit to data, K^S, $\mu_0 H^S$ and N_{eff} are included in Table 2. These values are approximate, as magnitudes depending on the applied field orientation are averaged and the considered nucleus shape is a prolate spheroid. It is found that the arrays exhibit negative effective demagnetizing factors N_{eff}, indicating that magnetostatic interactions tend to destabilize magnetization, decreasing the coercive force. The relative remanence curves are also consistent with the mechanism proposed and exhibit a maximum at $\varphi = 0$, indicating that the effective easy axis is parallel to the wire long axis.

The effective anisotropy fields of the investigated arrays, determined by applying the three magnetic techniques, are shown in Figure 7, together with the effective anisotropy field given by Eq. (2). The resulting values for the three characterization methods exhibit the same general trend as a function of composition, with a maximum for array Fe25. For similar aspect ratios (~ 260), the measured effective anisotropy fields increase with the iron content. On the other hand, in array Fe38 exhibiting the largest saturation magnetization value but containing NWs with (quite) smaller aspect ratio (~ 50), the anisotropy fields are lower, indicating that weaker shape effects largely reduce the effective anisotropy.

It may also be observed in Figure 7 that $\mu_0 H^L$ and $\mu_0 H^S$ resulting from DC techniques are relatively close to each other for arrays of all compositions. These values are comparable to those previously reported for Permalloy NWs [38] measured with DC methods and also for anisotropy fields determined with FMR [15, 20]. On the contrary, in the present work, the fields arising from FMR measurements, $\mu_0 H^{FMR}$, are quite smaller than those resulting from DC techniques.

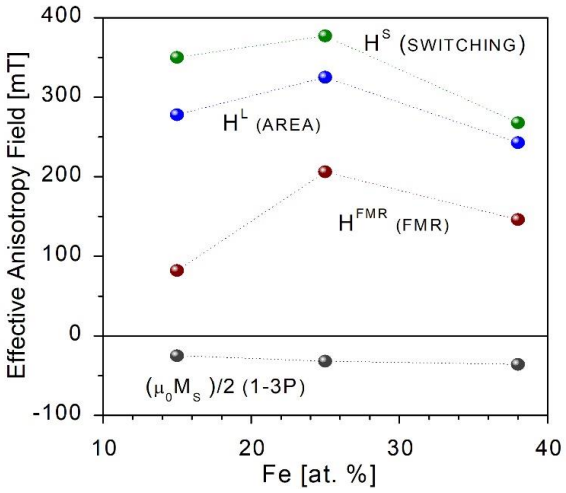

Figure 7. Different effective anisotropy field values in the arrays, determined by the three methods —by applying the area method to evaluate quasistatic hysteresis in the major hysteresis loops; through FMR measurements; and the effective anisotropy field acting during the magnetization switching mechanism responsible for coercivity. Field values calculated using Eq. (2), considering only magnetostatic interactions in porous systems are also shown.

Then, the main question becomes why in our arrays the effective anisotropy values determined by DC methods are systematically higher than those obtained from FMR measurements, with this difference not observed in other Fe-Ni NW arrays.

As mentioned above, previous experiments [30, 31] performed to compare FMR and $M(H)$ results show a much closer match between the effective fields resulting from these two measuring conditions. In these experiments, NWs with smaller radii (typically 35 nm or below) are measured, in which more uniform magnetization modes are likely to take place and dipolar interactions are relatively low. These factors, a more uniform magnetic structure and weak dipolar interactions, are likely to be responsible for the similar anisotropy values reported for FMR and $M(H)$ techniques [30, 31], in contrast with our present results. The relevance of the NW diameter in soft arrays is also evidenced by micromagnetic calculations related to the magnetization process in Ni NWs [39], which predict a transition in the predominant reversal mechanism at diameters of about D = 42 nm, with the system changing from a simple domain wall that nucleates and propagates along the wire axis to a reversal mechanism for thicker wires via a localized curling mode. Dipolar interaction between NWs would need to be considered in an extended micromagnetic model that

would describe the appropriate modes excited in FMR (similar to what has been done in small nanopillar arrays [40]) and DC magnetization reversal that would explain the observed differences in the effective anisotropy in these systems.

The porosity *P* of our samples is also larger than that reported in [30, 31], leading to stronger dipolar interactions between the wires in the array. However, it is remarkable that no negative values for the effective anisotropy field are obtained in our work, even when the traditional expression for magnetostatic interactions in porous systems [18] yields negative effective anisotropy values for porosities above 30% (see Figure 7).

Then, our results suggest that different/additional contributions to the effective anisotropy field must be involved in the static and dynamic $M(H)$ and FMR processes in large diameter NW arrays, and that they must be considered to better describe the observed anisotropy behavior. The interplay between magnetostatic interactions at different size scales (governed by diameter, porosity and composition) and the dynamic character of the magnetic microstructures in the arrays are likely to be responsible for the new contributions needed to understand our results.

4. Conclusion

The effective magnetic anisotropy field of Fe-Ni NW arrays was determined under three experimental conditions (quasistatic magnetization evolution along major hysteresis loops; ferromagnetic resonance at 34 GHz; and magnetization reversal by nucleation of inverse domains). It is found that the key parameters governing the effective anisotropy value are the alloy iron content, the mean wire diameter and length, and the array porosity.

The effective anisotropy field measured during $M(H)$ magnetization processes is higher by a factor of about 1.5 to 2 than that measured with FMR techniques. In all the three arrays a uniaxial easy axis along the nanowires axis was found, with no evidence of an easy plane behavior, as theoretically predicted for high porosity arrays as is the present case. These results indicate that new internal degrees of freedom need to be considered, in addition to the shape magnetostatic contribution and dipolar interactions, to understand the different effective anisotropy values measured in quasistatic hysteresis loops, during polarization reversal near coercivity and in ferromagnetic resonance dynamic processes.

Acknowledgements

This work has been partially funded by Secyt-UNC, ANPCyT-FONCyT and Conicet (Argentina).

CRediT authorship contribution statement

Joaquín Almeira: Methodology, Validation, Formal analysis, Investigation, Writing – original draft. Fernando Meneses: Validation, Investigation, Formal analysis. Julián Milano: Methodology, Validation, Investigation, Writing – review & editing. Carlos Ramos: Methodology, Validation, Investigation, Formal analysis, Writing – review & editing. Silvia E. Urreta: Conceptualization, Methodology, Formal analysis, Visualization, Writing – original draft, review & editing. Paula G. Bercoff: Conceptualization, Methodology, Formal analysis, Resources, Supervision, Validation, Visualization, Project administration, Funding acquisition, Writing – original draft, review & editing.

All authors read and approved the final manuscript.

Declaration of Competing Interest

The authors declare that they have no known competing financial interests or personal relationships that could have appeared to influence the work reported in this paper.

Data availability

The data that support the findings of this paper are available from the corresponding author upon reasonable request.

References

[1] H. D. Arnold, G. W. Elmen. Permalloy, A New Magnetic Material of Very High Permeability, Bell System Technical Journal 2 3 (1923) 101-111.

[2] C-W. Yang, D. B. Williams, J. I. Goldstein. A revision of the Fe-Ni phase diagram at low temperatures (< 400 C), *Journal of phase equilibria* 17 6 (1996) 522-531.

[3] L. F. Yin, D. H. Wei, N. Lei, L. H. Zhou, C. S. Tian, G. S. Dong, X. F. Jin, L. P. Guo, Q. J. Jia R. Q. Wu. Magnetocrystalline Anisotropy in Permalloy Revisited, *Phys. Rev. Lett.* 97 (2006) 067203.

[4] A. R. Balakrishna, R. D. James. A solution to the permalloy problem—A micromagnetic analysis with magnetostriction, *Appl. Phys. Lett.* 118 21 (2021) 212404.

[5] R. C. O'Handley. *Modern Magnetic Materials Principles and Applications* (2000) John Wiley \& Sons New York.
[6] S. A. Wolf, D. D. Awschalom, R. A. Buhrman, J. M. Daughton, S. von Molnár, M. L. Roukes, A. Yu Chtchelkanova, D. M. Treger. Spintronics: a spin-based electronics vision for the future, *Science* 294 5546 (2001) 1488—1495.
[7] E. Berganza, M. Jaafar, C. Bran, J. A. Fernández-Roldán, O Chubykalo-Fesenko, M. Vázquez, A. Asenjo. Multisegmented nanowires: A step towards the control of the domain wall configuration, *Scientific Reports* 7 1 (2017) 1-8.
[8] S. Parkin, M. Hayashi, L. Thomas. Magnetic domain-wall racetrack memory, *Science* 320 5873 (2008) 190-194.
[9] U. Yogeswaran, S-M. Chen, A review on the electrochemical sensors and biosensors composed of nanowires as sensing material, *Sensors* 8 (2008) 290-313.
[10] J. F. Fennell Jr, S. F. Liu, J. M. Azzarelli, J. G. Weis, S. Rochat, K.A. Mirica, ... & T.M. Swager, Nanowire chemical/biological sensors: Status and a roadmap for the future. *Angewandte Chemie International Edition*, 55(4) (2016) 1266-1281.
[11] G. Zhou, L. Xu, G. Hu, L. Mai, Y. Cui. Nanowires for electrochemical energy storage, *Chemical reviews* 119 20 (2019) 11042-11109.
[12] A. Mukhtar, K. Wu, X, Cao, and others. Magnetic nanowires in biomedical applications, *Nanotechnology* 31 43 (2020) 433001.
[13] M. M. Khin, A. S. Nair, V. J. Babu, R. Murugan, S. Ramakrishna. A review on nanomaterials for environmental remediation, *Energy & Environmental Science* 5 8 (2012) 8075-8109.
[14] M. Alikhani, A. Ramazani, M. Almasi Kashi, S. Samanifar, A. H. Montazer. Irreversible evolution of angular-dependent coercivity in $Fe_{80}Ni_{20}$ nanowire arrays: Detection of a single vortex state *J. of Magn. Magn. Mater*. 414 (2016) 158–167.
[15] M. Pardavi-Horvath, P. E. Si, M. Vázquez, W. O. Rosa, G. Badini. Interaction effects in Permalloy nanowire systems, *J. Appl. Phys.* 103 (2008) 07D517.
[16] M. Demand, A. Encinas-Oropesa, S. Kenane, U. Ebels, I. Huynen, L. Piraux. Ferromagnetic resonance studies of nickel and permalloy nanowire arrays, *J. of Magn. Magn. Mater*. 249 (2002) 228–233.
[17] A. Encinas-Oropesa, M. Demand, L. Piraux, U. Ebels, and I. Huynen. Effect of dipolar interactions on the ferromagnetic resonance properties in arrays of magnetic nanowires, *J. Appl. Phys.* 89 (2001) 6704.
[18] A. Encinas-Oropesa, M. Demand, L. Piraux, I. Huynen and U. Ebels,. Dipolar interactions in arrays of magnetic nanowires studied by ferromagnetic resonance, *Phys Rev. B.* 63 (2001) 104415.
[19] J. M. Martínez Huerta, J. De La Torre Medina, L. Piraux, A. Encinas. Self-consistent measurement and removal of the dipolar interaction field in magnetic particle assemblies and the determination of their intrinsic switching field distribution, *J. Appl. Phys.* 111 (2012) 083914.
[20] V. Raposo, M. Zazo, A. G. Flores, J. Garcia, V. Vega, J. Iñiguez, V. M. Prida. Ferromagnetic resonance in low interacting permalloy nanowire arrays, *J. Appl. Phys.* 119 (2016) 143903.
[21] H. Masuda and K. Fukuda. Ordered Metal Nanohole Arrays Made by a Two-Step Replication of Honeycomb Structures of Anodic Alumina, *Science* 268 5216 (1995) 1466-1468.
[22] K. Nielsch, F. Müller, A-P. Li, U. Gösele. Uniform nickel deposition into ordered alumina pores by pulsed electrodeposition, *Advanced Materials* 12 8 (2000) 582-586.
[23] A. L. Patterson. The Scherrer formula for X-ray particle size determination, *Physical Review* 56 10 (1939) 978.
[24] J. S. Kasper, K. Lonsdale. *International Tables for X-Ray Crystallography*, Volume II (1972) Kinoch Press, Birmingham, UK.
[25] D. Bastian, E. Biller. Anisotropy Constants and g-Factors of Ni-Fe Alloys Derived from Ferromagnetic Resonance, *Physica Status Solidi (a)* 35 2 (1976) 465-470.
[26] B. D. Cullity, C. D. Graham. *Introduction to Magnetic Materials*, Second Edition. Wiley-IEEE Press, March 2010.
[27] C. Vittoria. *Microwave properties of magnetic films.* (1993) World Scientific. https://doi.org/10.1142/2038
[28] S. M. Rezende. *Fundamentals of magnonics. Lecture Notes in Physics 969.* 1st Edition (2020) Springer.
[29] L-P. Carignan, C. Lacroix, and A. Ouimet, M. Ciureanu, A. Yelon, D. Ménard. Magnetic anisotropy in arrays of Ni, CoFeB, and Ni/Cu nanowire, *J. Appl. Phys.* 102 2 (2007) 023905.
[30] L. Forzani, A. M. Gennaro, and R. R. Koropecki, C. A. Ramos. Sensing anisotropic stresses with ferromagnetic nanowires, *Appl. Phys. Lett.* 116 1 (2020) 013104.
[31] M. S. Salem, K. Nielsch. Crossover between axial and radial magnetic anisotropy in self-organized permalloy nanowires, *Materials Science and Engineering: B* 223 (2017) 120-124.
[32] R. Skomski, H. Zeng, M. Zheng, and D. J. Sellmyer. Magnetic localization in transition-metal nanowires, *Physical Review B* 62 6 (2000) 3900-3904.
[33] E. C. Stoner, E. P. Wohlfarth. A Mechanism of Magnetic Hysteresis in Heterogeneous Alloys, *Philosophical Transactions of the Royal Society A*,

Mathematical and Physical Sciences 204 (1948) 599-642.
[34] A. Aharoni. Angular dependence of nucleation by curling in a prolate spheroid, *J. Appl. Phys.* 82 (1997) 1281.
[35] M. S. Viqueira, N. Bajales, S. E. Urreta, P. G. Bercoff. Magnetization mechanisms in ordered arrays of polycrystalline Fe_{100-x} Co_x nanowires, *J. Appl. Phys.* 117 (2015) 204302.
[36] S. Shtrikman and D. Treves, in Magnetism, edited by G. T. Rado and H. Suhl - Academic, New York, 1963, Vol. 3.
[37] A. Aharoni, S. Shtrikman, Magnetization curve of the infinite cylinder, *Phys. Rev.* 109 (1958) 1522–1528.
[38] M. S. Salem, P. Sergelius, R. Zierold, J. M. Montero Moreno, D. Görlitz, K. Nielsch. Magnetic characterization of nickel rich NiFe nanowires grown by pulsed electrodeposition, *J. Mater. Chem.* 22 (2012) 8549–8557.
[39] R. Hertel, J. Kirschner. Magnetization reversal dynamics in nickel nanowires. *Physica B* 343 (2004) 206–210.
[40] J. F. O. da Silva, E. Padrón-Hernández. Effects of the packing factor on magnetic anisotropy in a 3x3 array of square hollow Ni nanopillars, *J. Mag. Mag. Mat.* 551 (2022) 169175.

Supplementary Information

Nanowires' composition

Fe15

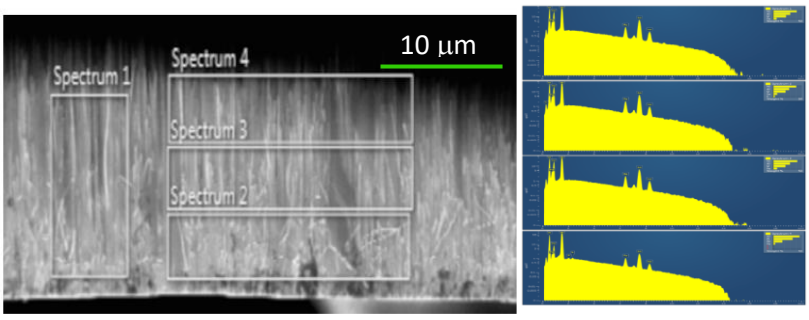

Figure S1. EDS spectra corresponding to the zones delimited by rectangles in the left SEM image. Sample Fe15.

Table S1, Fe and Ni concentration in at.% corresponding to different zones explored

	Composition of Fe15 (at. %)									
	S1	S2	S3	S4	S7	S8	S9	S10	S2'	S4'
Fe	3.29	3.64	3.76	1.58	3.37	3.21	3.30	2.41	1.38	1.65
Ni	21.10	19.88	21.86	6.55	18.44	18.06	19.57	14.74	7.00	7.48

Fe25

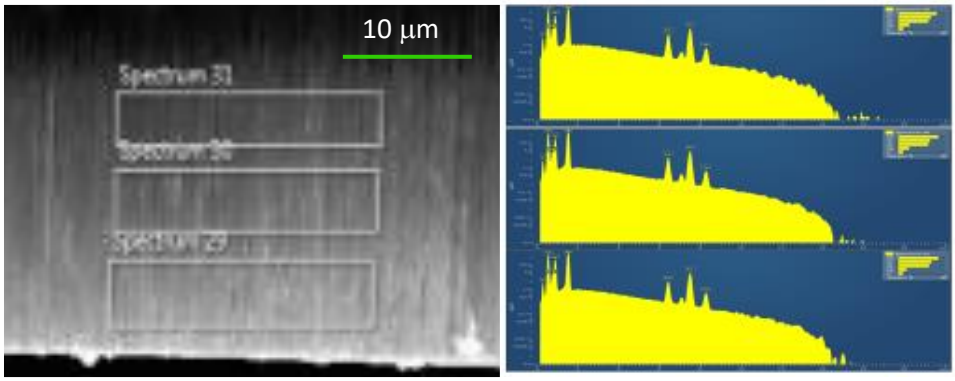

Figure S2. EDS spectra corresponding to the zones delimited by rectangles in the left SEM image. Sample Fe25

Table S2. Fe and Ni concentration in at.% corresponding to different zones explored

	Composition of Fe25 (at. %)								
	bottom			middle			top		
	S26	S29	S32	S27	S30	S33	S28	S31	S34
Fe	4.17	4.65	3.55	4.93	4.56	4.09	2.85	3.60	2.72
Ni	15.45	14.53	10.06	14.41	15.30	11.23	17.44	15.09	12.43

Fe38

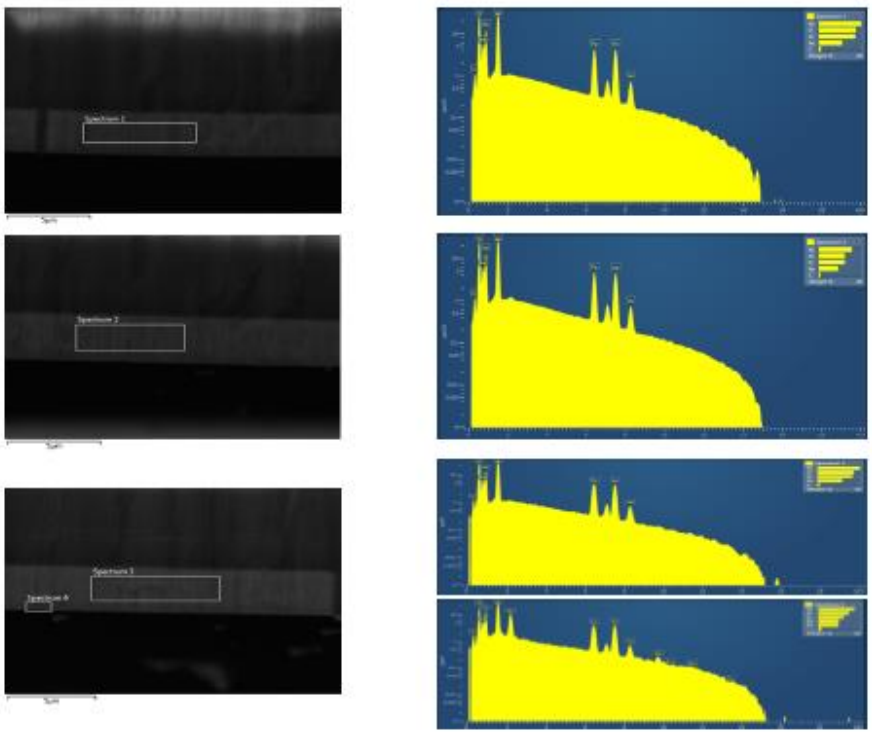

Figure S3. EDS spectra corresponding to the zones delimited by rectangles in the left SEM image. Sample Fe38.

Table S3. Fe and Ni concentration in at.% corresponding to different zones explored

	Composition Fe38 (at. %)					
	S1	S2	S3	S4	S5	S6
Fe	8.29	9.29	8.92	8.72	8.77	8.59
Ni	14.28	15.22	14.48	14.95	14.25	13.58

Table S4, Mean value of Fe concentration (balance Ni) , corresponding to different samples

Sample	Mean Fe at. % (balance Ni)
Fe15	15±1
Fe25	25±1
F338	38±1